



HAL
open science

Survivability of the thermographic phosphors YAG:Pr and SMP:Sn in a premixed flame

Andreas Kopf, Michele Bardi, Eric Kohler, Torsten Endres, Gilles Bruneaux,
Christof Schulz

► **To cite this version:**

Andreas Kopf, Michele Bardi, Eric Kohler, Torsten Endres, Gilles Bruneaux, et al.. Survivability of the thermographic phosphors YAG:Pr and SMP:Sn in a premixed flame. *Measurement Science and Technology*, 2021, 32 (7), pp.074001. 10.1088/1361-6501/abf57b . hal-03248559

HAL Id: hal-03248559

<https://ifp.hal.science/hal-03248559>

Submitted on 3 Jun 2021

HAL is a multi-disciplinary open access archive for the deposit and dissemination of scientific research documents, whether they are published or not. The documents may come from teaching and research institutions in France or abroad, or from public or private research centers.

L'archive ouverte pluridisciplinaire **HAL**, est destinée au dépôt et à la diffusion de documents scientifiques de niveau recherche, publiés ou non, émanant des établissements d'enseignement et de recherche français ou étrangers, des laboratoires publics ou privés.

Survivability of the thermographic phosphors YAG:Pr and SMP:Sn in a premixed flame

A. Kopf^{1,2,*}, M. Bardi¹, E. Kohler¹, T. Endres², G. Bruneaux¹, C. Schulz²

¹IFP Energies Nouvelles, 1 et 4 Avenue de Bois-Préau, 92852 Rueil-Malmaison Cedex, France; Institut Carnot IFPEN Transports Energie

²IVG, Institute for Combustion and Gas Dynamics – Reactive Fluids, and CENIDE, Center for Nanointegration, University of Duisburg-Essen, Germany

Abstract

The survivability of two thermographic phosphors, YAG:Pr³⁺ and SMP:Sn ((Sr,Mg)₃(PO₄)₂:Sn²⁺), in a combustion environment is studied in the post-flame regime of a premixed propane/air flame. While the laser-induced luminescence of YAG:Pr can be exploited for *in situ* temperature measurements in the exhaust gas above the flame, there is no *in situ* detectable luminescence for SMP:Sn for any reaction conditions within the stability limits of the flame. The phosphor particles are recaptured above the flame and *ex situ* analyzed for chemical or structural changes using microscopic analysis (SEM/EDX) and X-ray diffraction. The microscopic analysis of post-flame YAG:Pr does not show any alteration, whereas morphology and chemical composition of SMP:Sn have been modified upon passing through the reaction zone, which is responsible for the loss of its luminescence properties.

Keywords: YAG:Pr, tin-activated strontium magnesium phosphate (SMP:Sn), survivability, phosphor thermometry, *in situ* combustion temperature imaging

1. Introduction

Thermographic phosphors enable the remote measurement of temperature based on the temperature dependent variation in laser-induced luminescence spectra or signal lifetime. They have been frequently used for surface temperature measurements [1] but recently, applications have been extended to gas-phase temperature imaging measurements based on aerosolized phosphor particles [2]. This approach is of particular interest in reacting flows, where frequently used molecular species for thermometry (such as organic tracers [3, 4] or small molecules (e.g., NO [5, 6]) can be affected in the reaction medium or restricted to the area where radicals naturally occur (e.g., OH [7, 8]). Thermographic phosphors that survive the flame environment enable temperature measurements in the gas phase before and behind the flame front, which is of specific interest, e.g., in the context of

understanding in-cylinder processes in internal combustion engines. Thermographic phosphors with strong luminescence and short radiative lifetimes are required for temperature measurements in reacting gas flows to provide signal that can be discriminated against background luminescence, e.g., from a flame. For the selection of an appropriate thermographic phosphor, it is equally important that the emission properties of the phosphor are strongly temperature sensitive to obtain good measurement precision. It is of interest to cover flame temperature as well as areas that have been exposed to a flame in the process but cooled down again (e.g., in the expansion stroke). There are two limitations to applications of thermographic phosphors in such an environment: (i) Weak signal at high temperature that then is in competition with flame chemiluminescence and particle thermal radiation, and (ii) Potential disintegration of materials in the flame zone due to high temperature and through exposure to oxidizing species.

To overcome the first limitation, a new approach for phosphor thermometry was recently presented using the ratio of the temperature-sensitive phosphor luminescence and the temperature-insensitive Mie-scattered laser light for temperature sensing (scattering-referenced aerosol phosphor thermometry, SRAPT) [9]). This strategy extends the measurable temperature range to 1000 K at a single-shot precision better than 4% with a temperature sensitivity up to $1.6\%K^{-1}$. Overcoming the second limitation of disintegration of the phosphor depends on the respective materials properties. A large range of phosphor materials has been investigated for thermometry purposes in various applications, (Sr,Ca)SiAlN₃:Eu²⁺ [10], LuAG:Pr³⁺,Ce³⁺ [11], YAG:Pr³⁺,Ce³⁺ [12], YAG:Pr³⁺ [13], (Sr,Mg)₃(PO₄)₂:Sn²⁺ [14], but only few aerosolized thermographic phosphors have been reported to withstand combustion. BAM:Eu²⁺ maintains its luminescent properties upon passing through a laminar non-premixed flame [15]. It was also used for temperature imaging measurements in the residual gas of a high-pressure combustion cell [16]. YAG:Dy³⁺ was successfully applied for thermographic measurements in an HCCI combustion in an engine [17]. The luminescent properties of the same phosphor were also unaffected by passing the flame front of a premixed methane/air flame [18].

This work evaluates the applicability of (Sr,Mg)₃(PO₄)₂:Sn²⁺ and YAG:Pr³⁺ for thermometry applications in the post-combustion region. Both phosphors are highly sensitive to a change in temperature in the order of $0.5\text{--}0.8\%K^{-1}$ in the range of temperatures relevant for reacting flow conditions (600–900 K) [2, 14, 19]. The emission lifetime ($1/e$) of both phosphors is on the order of $\sim 1\ \mu\text{s}$ (SMP:Sn) and $60\ \mu\text{s}$ (YAG:Pr, ³P_J transition) in the aforementioned temperature range [14, 19, 20]. This is convenient for the application in reacting flows, as it is short enough to capture temperature changes on timescales relevant to, e.g., internal combustion engines. At the same time, it is long enough to enable the suppression of short-lived fluorescence contributions from intermediate species by delaying the detection time by a few tens of nanoseconds. Praseodymium-doped yttrium aluminum garnet (YAG:Pr³⁺) shows non-radiative and radiative relaxation from the excited 4f–5d levels to the ³P_J ($J = 0, 1, 2$) and the ¹D₂ state, which de-excite to the ³H₄ ground state [21], emitting in two visible narrow emission bands, centered at 489 and 610 nm respectively. Pr³⁺ emissions were reported to have emission rates greater than unity for visible emissions due to cascade processes [22]. At increasing temperatures, the ³P_J transition is quenched most likely due to multiphonon relaxation [23], which can be exploited for temperature sensing: The temperature is measured by calculating the intensity ratio between the two emission bands, which is also known as the two-color method or intensity-ratio approach. Due to thermal quenching of this blue emission this technique is limited as the signal decreases

to noise level. The intensity-ratio approach has been applied for 2D temperature imaging in a heated jet [13] and during the compression stroke in a Diesel engine [19] due to favorable luminescent properties such as high emission intensities and relatively short radiative lifetimes, but not reported for temperature measurements in the post-combustion regime. The melting point of YAG is $2213\pm 7\ \text{K}$ [24].

(Sr,Mg)₃(PO₄)₂:Sn²⁺ (in this work referred to as SMP:Sn) is a tin-activated ternary orthophosphate, where strontium can partly be replaced and stabilized with zinc or alkaline earth metal ions (Ba, Ca, Mg) to improve luminescence [25]. The luminescence strongly depends on the host lattice. The lattice provides two possible sites with distinct coordination numbers for divalent cations like Sn²⁺ and it was found that the different coordination numbers of the luminescent centers are responsible for two separate emission bands, following UV excitation [26]. This phosphor exhibits a major yellow-red emission band centered at 610 nm at room temperature from luminescence centers of high coordination numbers, and a near-UV emission band at 400 nm from lower coordination. The latter only accounts for 5 % of the total emission energy and disappears at increasing temperatures [26, 27]. With increasing temperatures, the yellow-red broadband emission shows a pronounced redshift, which can be used for thermometry purposes using the intensity-ratio approach.

In a mixed (Sr,Mg)-orthophosphate such as the SMP:Sn phosphor, the luminescence depends on the amount of Mg that replaces Sr in the crystal lattice. In the phase diagram of the mixed orthophosphate Sr₃(PO₄)₂ – Mg₃(PO₄)₂, provided by Sarver et al. [28], it is shown that the phosphate forms solid solutions during cooling at room temperature, as the mole percentage of the Mg₃(PO₄)₂ is increased from 0 % (pure Sr₃(PO₄)₂) to 100 % (pure Mg₃(PO₄)₂). For example, the crystal phase of the (Sr,Mg)-phosphate for a Mg₃(PO₄)₂ mole fraction of 10–35% is annotated in this publication as β -Sr₃(PO₄)₂, even if it refers to the β -phase of the mixed (Sr,Mg)-phosphate. For simplification, the nomenclature in this work will be aligned with the one of the references. The Mg₃(PO₄)₂ mole fraction leading to the phosphors' highest brightness is around 10–15%, where the crystal structure of the phosphate is β -Sr₃(PO₄)₂. At increasing mole fractions of the strontium phosphate (<10% Mg₃(PO₄)₂), the phase diagram shows a two-phase region of α - and β -Sr₃(PO₄)₂, where the α -Sr₃(PO₄)₂ is non-luminescent but has low ultraviolet absorption, emphasizing the strong sensitivity of the lattice composition to luminescence. The melting temperature of SMP:Sn is not exactly known but specified by the manufacturer to be above 1473 K [29]. This phosphor has first been characterized for thermometry purposes by Fond et al. and shows promising luminescent properties for

thermometric applications, relatively to BAM:Eu²⁺ or ZnO, due to a low cross-dependency to laser fluence at similar global emission intensities (photons per particle per pulse) [14, 30].

This study evaluates the two phosphors YAG:Pr and SMP:Sn for thermographic measurements in reacting conditions of a premixed propane/air flame. Temperature imaging measurements exploit the signal ratio of two emission bands that are determined by optical filters. At increasing temperatures, the emission spectra shift towards shorter wavelengths (e.g., for SMP:Sn) or the intensity of the emission bands are differently affected from thermal quenching (e.g., for YAG:Pr), leading to varying signal ratios. The temperature can be inferred from a calibration curve, where the signal ratio of both emission bands is calibrated at known temperatures.

2. Materials and experimental methods

We use an in-house built premixed burner (outlet nozzle $d = 12$ mm) with a passive co-flow and chimney extension, which is needed to stabilize the flow further downstream of the flame. The stabilizing inert co-flow is controlled with inlet flaps on the bottom of the burner housing. Increasing co-flow stabilizes the flow by reducing shear between the two flows and thus natural convection between both flows. The measurable region is located at the chimney outlet 175 mm above the burner nozzle, where phosphor particles are seeded into the oxidizer flow. The fuel/air equivalence ratio ϕ of a premixed propane/air flame is varied between 0.62 and 1.0 to change the flame temperature and thus the temperature of the exhaust gases. The adiabatic flame temperatures for the respective equivalence ratios range from 1650 to 2350 K [31].

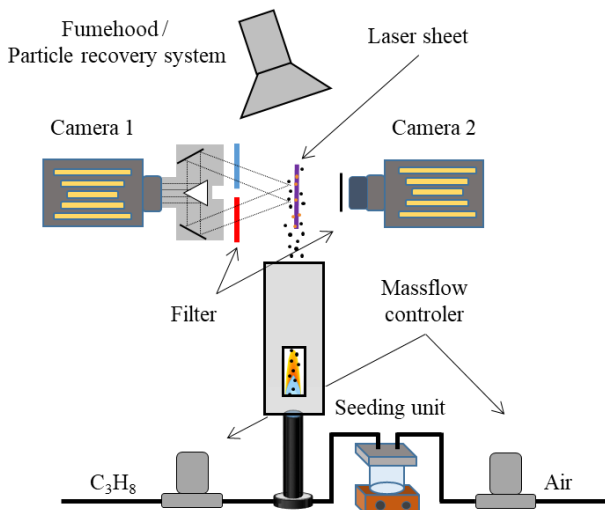


Figure 1: Arrangement for thermographic measurements in the post-combustion zone of a premixed burner.

YAG:Pr is provided by Phosphor Technology (QMK59/F-X #29010, $d_{50} = 4.2$ μm) with a dopant concentration of 0.5 % similar to that used in previous measurements that investigated the temperature dependence of the luminescence [13]. Additionally, SMP:Sn, a phosphor from OSRAM GmbH that is used commercially in color rendering lamps (SV 253 #B4640219, $d_{50} = 8 \dots 10$ μm) was investigated after it was grinded and de-agglomerated to a diameter of $d_{50} = 1.6$ μm .

Two-color phosphor thermometry is carried out in the post-combustion zone above the flame, where the flow has cooled down. A Nd:YAG laser is quadrupled to the fourth harmonic (266 nm) and a combination of a cylindrical and a spherical lens is used to form a light sheet 65 mm wide and approx. 0.5 mm thick (90 mJ/cm²). An intensified camera (PIMax 4, EmCCD, 16 bit, intensifier gen2) is equipped with an image splitter (LaVision, ImageDoubler) to project an identical image pair of one object through two optical filter sets onto a single camera chip. The camera detection gate for the phosphorescence detector (camera 1) was set to 50 μs and delayed by 100 ns relatively to the laser pulse, similar to comparable imaging experiments [13]. An identical camera is used for Mie-imaging (camera 2). The filters employed for thermometry are a Semrock bandpass filter FF01-494/20 (blue channel) and a combination of Schott colored glass OG570 and a 625 nm shortpass filter (Edmund Optics #64-604) for the red channel. The spatial fluctuations of the gas flow above the burner as well as instabilities in the particle seeding require a large data set of 1000 images. To account for these instabilities, the intensity ratio map is calculated for every image after applying a cutoff filter (<600 counts), spatial averaging (3×3 pixels) on both images and dividing it by the average ratio taken at ambient temperature in inert flow conditions. The temperature field is then obtained using a calibration curve obtained in a furnace [13]. The gas temperature is also measured with thermocouples (type K, 1.0 mm tip diameter). The phosphor particles are collected on a filter membrane above the burner for microscopic analysis, where the filter support is inserted in the exhaust ventilation system.

2.1. Particle residence time

The residence time of the phosphor particles in the flame at certain conditions (oxidizing environment, high temperature) is of interest in order to estimate the potential disintegration of phosphor particles in other practical environments (e.g., IC engines). For example, if the temperature of the particle-laden gas surpasses melting temperature of the phosphor material, but the residence time at this temperature is shorter than the time required for heat conduction, temperature measurements can be unaffected in the post-flame regime.

2.1.1 Numerical simulation

For calculating the residence time, a 2D axisymmetric steady-state numerical simulation was carried out in Ansys Fluent. The passive co-flow of the chimney housing is accounted for with a co-flow (air) around the burner central flow (propane & air). The boundary conditions for the inlet velocity are calculated from the measured mass flows of propane and air and the mass flow of the surrounding co-flow is adapted in the simulation to generate the best match with the temperature values measured by thermocouples in the exhaust gas. Gravitation is neglected, as well as radiation effects from the burner chimney. The reaction kinetics are calculated with the CHEMKIN CFD solver using the complete San Diego mechanism [32].

The residence time of a particle at high temperature is derived from the simulated temperature and gas velocity in the flame. Figure 2 shows the accumulated time a particle is exposed to a certain temperature or above on its path through the flame. The evolution of temperature and gas velocity over time are also shown for completeness. The time a phosphor particle is exposed to temperatures above 1473 K (melting temperature specified by the manufacturer is $T > 1473$ K [29]) is 38 ms. Temperatures above 1920 K are reached for 0.9 ms.

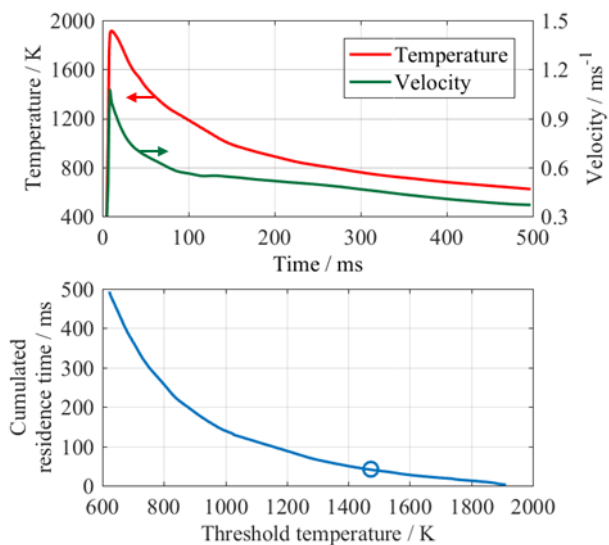


Figure 2: Top: Temperature and gas velocity over time of a particle through the flame. Bottom: Cumulative residence time of a particle at a given temperature or above in a premixed propane/air flame ($\phi = 0.71$). The residence time for $T \geq 1473$ K is highlighted with a circle.

Theoretical heat transfer considerations on the response time t_{95} until a particle reaches 95 % of the steady-state temperature following a step temperature change of the surrounding gas temperature is below $30 \mu\text{s}$ [33]. The considerations were made for a $2\text{-}\mu\text{m}$ phosphor particle (YAG) for a step change from 300 to 2000 K, which is representative for combustion conditions. Because the time scale for thermal equilibration is three orders of magnitude

shorter than the residence time of the particle in the high-temperature zone in the flame, the particles are expected to reach steady-state temperature. Assuming that the melting temperature for SMP:Sn ($T > 1473$ K [29]) is reached, the residence time at this temperature is long enough to expect complete melting. A more detailed discussion about the expected melting temperature can be found in section 3.3.

3. Results and discussion

3.1. Exhaust gas temperature measurements

The objective of the following measurements is to investigate, whether the phosphors maintain their temperature-dependent spectroscopic properties after having been exposed to the flame. Temperature measurements in the post-combustion gases are carried out employing the two-color thermometry approach using YAG:Pr. Figure 3 shows a single shot image of both imaging channels. The blue channel suffers from thermal quenching and is thus the limitation for statistically significant measurements at high temperatures. The signal to noise ratio (SNR) is evaluated based on the 90th and the 10th percentile of the signal intensities in the respective region of interest. The signal was calculated in the hottest region in the center of the gas flow (red box) and the noise was estimated from a region outside the flow (yellow box).

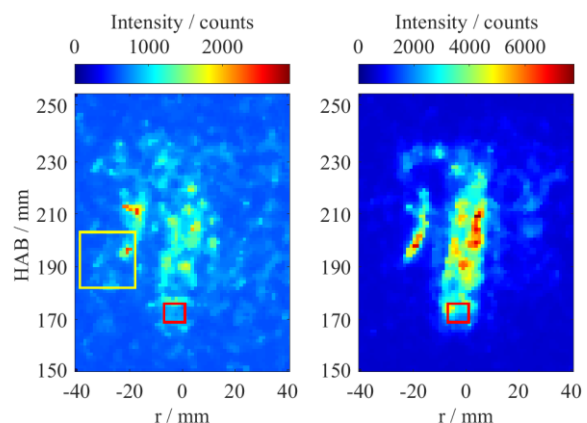


Figure 3: Single-shot images of the blue (left) and red (right) channel in the exhaust gas at $\phi = 1.0$. The red and the yellow box highlight the regions used for SNR calculation. The intensity scale in each image was adjusted for improved visibility.

Figure 4 shows the temperature dependence of the signal-to-noise ratio for each individual signal channel. The low percentile threshold for noise calculation was chosen in order to be insensitive to varying signal contribution due to turbulent fluctuations, as can be seen in Figure 3.

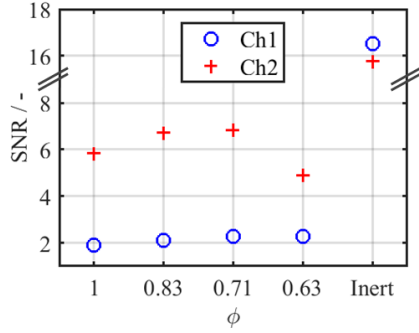


Figure 4: Signal-to-noise ratio for both imaging channels for various fuel/air equivalence ratios.

Following the procedure for image processing detailed in section 2, an intensity ratio and temperature map can be calculated from both channels. Averaged two-dimensional temperature map of the post-combustion gases above the burner, derived from YAG:Pr two-color thermometry measurements are shown in Figure 5 for fuel/air equivalence ratios of 0.83 (left) and 0.63 (right), showing that the leaner equivalence ratio results in lower exhaust gas temperatures. The flow is not axisymmetric due to the effect of the fume hood. The regions highlighted in gray are not considered for temperature calculation due to a light reflection from metal surfaces of the chimney. This optical artifact could be reduced using structured laser illumination [34], but is not the objective of this study.

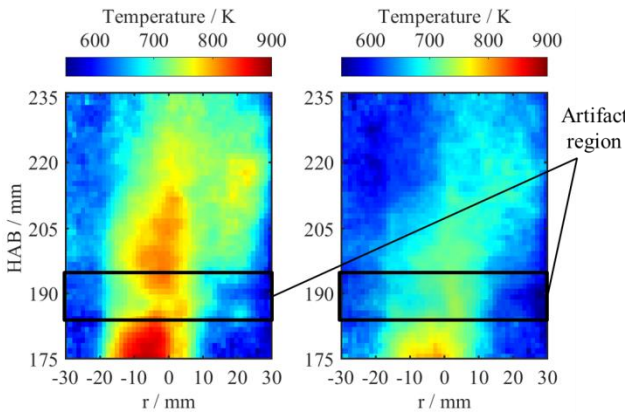


Figure 5: Average temperature field of the exhaust gas for $\phi = 0.83$ (left) and $\phi = 0.63$ (right) from two-color luminescence measurements using YAG:Pr.

Figure 6 shows the temperature profile extracted from the average temperature field and presents the gas temperature in vertical direction above the chimney outlet of the burner for varying fuel/air equivalence ratios. The temperature profile is averaged from three horizontally averaged pixels. The measured gas temperatures follow two trends, (i) decreasing gas temperature for decreasing ϕ and (ii) decreasing temperatures at increasing height above the burner (HAB)

and are in good agreement with thermocouple (TC) measurements. The error bars in the TC measurements represent the deviation from temperature measurements in the flow. Due to increasing spatial fluctuations downstream in the flow at increasing HAB, the error bar is larger at the upper thermocouple position (HAB = 225 mm).

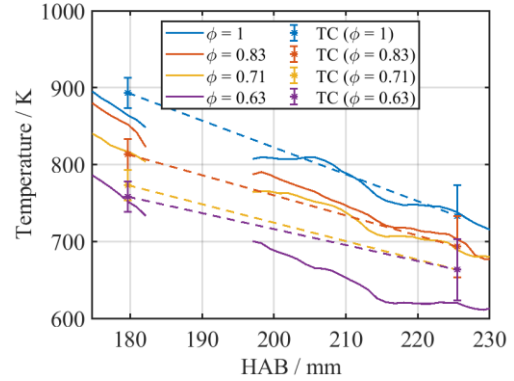


Figure 6: Temperature profiles from thermographic phosphor measurements above the burner along the vertical direction (solid lines) for various fuel/air equivalence ratios for YAG:Pr derived from the two-color luminescence measurements. TC: Thermocouple measurements with error bars.

Despite the uncertainties related to the thermocouple measurement, the flame fluctuations or limitation using the calibration acquired in a furnace, these results clearly show that YAG:Pr phosphor particles maintain its temperature-sensitive luminescence emission after passing the flame front of the burner.

A possible source of bias in the measurements could be black-body radiation related to the phosphor particles. Above a certain temperature this contribution will be non-negligible and will compete with the luminescence emitted by the phosphor, creating a bias in temperature measurements. However, in the current experimental conditions, this contribution is not expected to be significant for the following two reasons: Firstly, the consistency of the temperature measurements found over the entire temperature range and secondly the agreement with the TC measurements. This interference problem will be strengthened when extending the measurements to reacting conditions due to other competing luminescent signals, like chemiluminescence or soot incandescence.

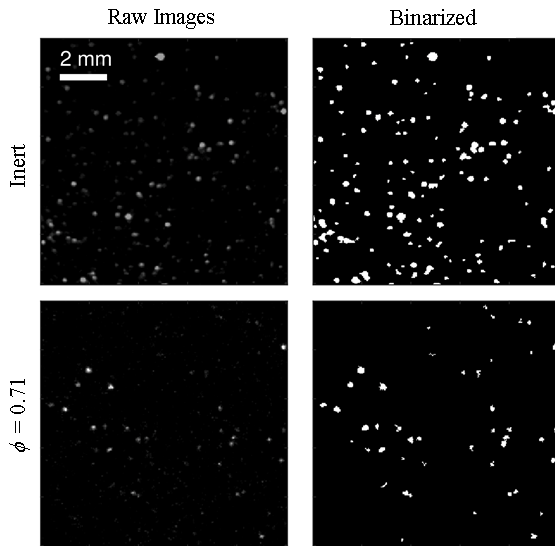


Figure 7: Raw (left) and associated binarized Mie- scattering images (right) for inert (top) and reacting (bottom) conditions for YAG:Pr.

Figure 7 shows a set of Mie-scattering images for inert and reacting flow conditions. With the binarizing threshold chosen for this study, the volumetric particle number density (PND) in the reacting conditions ($\phi = 0.71$) is a factor of 2.3 lower than in the inert flow, which is equivalent to the difference in gas density between 800 and 300 K. In the same temperature range, the band-integrated luminescence is expected to decrease by a factor of ~ 5 – 10 [20]. In our experiment, the volumetric luminescence decreased to $\sim 12.5\%$ in the hot case, which indicates that the observed effect results from a combination of density variation and thermal quenching and not to the total loss of luminescence due to particle degradation.

The second investigated phosphor SMP:Sn shows strong luminescence emission under inert conditions at ambient temperature, but does not exhibit any detectable phosphor luminescence in the post-combustion regime for any stable operating point tested in the burner ($\phi = 0.58$ – 1.25). Phosphor luminescence at similar temperatures (up to 873 K) was measured in inert conditions in a furnace on a coated surface [35]. Since particles were visible on the second camera (Mie-imaging), these results indicate particle degradation leading to a loss of the materials' luminescent properties upon passing the reaction zone of a premixed propane/air burner flame.

3.2. Ex situ particle analysis (SEM/EDX, XRD)

Microscopic particle analysis of the phosphor material is carried out using scanning electron microscopy (SEM) to investigate the impact of the exposure to the combustion environment on their morphology (secondary electrons detector, SE) or chemical composition (energy dispersive

spectroscopy, EDX). Initial measurements are carried out in bulk powder material with an acceleration voltage of 15 kV and an anode current of 750 pA (Zeiss, EVO MA10). EDX measurements of bulk material give an average chemical composition from the sample volume penetrated by the incident electron beam. As the penetration depths is not known, bulk powder measurements only allow a qualitative description of the chemical composition of the initial and post-flame material. For further analysis of the chemical composition, the SMP:Sn post-flame powder is embedded in epoxy resin and cut into thin slices using an ultra-microtome (Leica EM UC). The thickness of the slices is between 100 and 200 nm. Thus, the electron penetration depth is expected to be constant for any point in the cross-section of a particle. The chemical composition of the particle cross-sections is analyzed using an EDX detector (Bruker, XFlash 6I10 SDD) built into an Auger microscope (Ulvac-Phi, Phi 710 Nanoprobe).

The phosphor particles were captured approx. 300 mm above the burner nozzle after passing through a $\phi = 0.71$ flame with an adiabatic flame temperature of ~ 1900 K [31]. The crystal structure of both, initial and post-flame powder is analyzed using an X-ray powder diffractometer (Bruker, D8 Discover) to investigate structural changes of the lattice or the presence of newly formed solids from alteration due to flame exposure.

The results from both techniques are presented individually for both phosphors in 3.2.1 and 3.2.2. and then discussed together in section 3.3.

3.2.1 YAG:Pr

Figure 8 shows the SEM image from initial and post-flame material. Images from the initial material show mostly sharp-edged particles that formed small agglomerates. Apart from few isolated spherical particles, YAG:Pr does not show any morphological alteration in the post-flame material. Results from EDX measurements do not show a statistically significant modification in chemical composition in the host material ($Y_3Al_5O_{12}$) of the post-flame YAG:Pr from the initial material. The concentration of the praseodymium ion doped into the host lattice is too low to be measured.

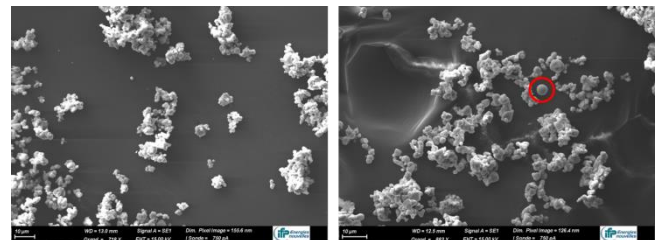


Figure 8: SEM image of initial (left) and post-flame (right) YAG:Pr particles. A spherical particle is highlighted by a circle.

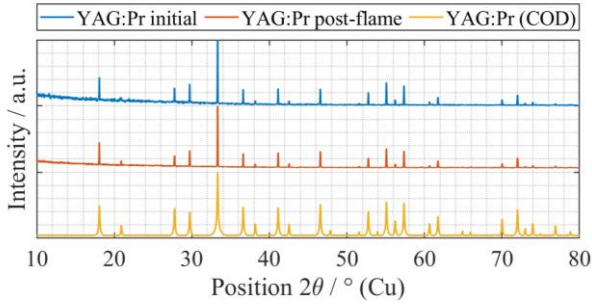


Figure 9: Diffraction pattern from initial and post-flame YAG:Pr phosphor material with its COD reference pattern from [36]. The diffraction pattern from the COD reference is calculated using the same copper anode (1.5406 Å) as used for the XRD measurements. Intensities are normalized towards the intensity of the highest peak.

The X-ray diffraction pattern (Figure 9) of the post-flame powder does not show any changes relatively to initial material and is in excellent agreement with the reference diffraction pattern [36] calculated with crystallographic information from the crystallographic open database (COD# 1529037) [37]. This confirms that the crystal structure remains unchanged after passing the flame front under the given conditions.

3.2.2 SMP:Sn

SEM-measurements of the morphology of particles from the post-flame SMP:Sn phosphor show severe changes relatively to the initial sharp-edged material, where the large majority of the post-flame particles are characterized by a spherical shape (Figure 10, right). The chemical composition from EDX measurements in the initial material is $\text{Sr}_{2.62}\text{Mg}_{0.38}(\text{PO}_4)_2 \cdot \text{Sn}^{2+}$, which is equivalent to 12.5 mol% $\text{Mg}_3(\text{PO}_4)_2$. The post-flame material is slightly enriched in the relative strontium content $\text{Sr}_{2.66}\text{Mg}_{0.34}(\text{PO}_4)_2 \cdot \text{Sn}^{2+}$ (11.3 mol% $\text{Mg}_3(\text{PO}_4)_2$). These preliminary results confirm a qualitative modification on the structure from the exposure to the flame. As EDX provides semi-quantitative analysis only, the small change in chemical composition on a particle basis should be interpreted with care. The modification of the shape of the grains towards a spherical shape indicates a transformation to the liquid state in the flame. The return to the solid state does not seem to be accompanied by a general phase demixing since the change in chemical composition is low compared to the initial state.

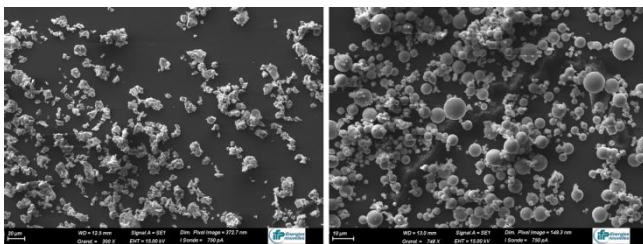


Figure 10: SEM image of initial (left) and post-flame (right) SMP particles.

Figure 11a shows the secondary electron (SE) image of the cross-section, representing the topographic map of the particles. Any structure visible in a particle in (a), apart from preparation artifacts, is attributed to a locally varying surface topography. It is also possible that the surface irregularities cause EDX analysis artifacts specific to each chemical species. The gradient in the particle (3) is due to shading effects as confirmed from a series of rotated images. The inhomogeneities on the particles, annotated as (1) and (2), thus stem from locally varying materials properties, which could become visible in the topographic image from being differently displaced by the microtome blade, likely due to changed crystal phase properties. Figure 11c–f shows the relative distribution of the chemical species of SMP:Sn. Particles (1) and (2) show a mostly homogeneous distribution of both the phosphate (P, O) as well as Mg, whereas there are spots with relatively increased Sr concentration. Figure 11b shows an overlaid SE/EDX image, where regions of varying material properties are highlighted. These regions with increased Sr concentration, numbered in white in Figure 11b show a mean Sr content of 52.8 wt%. Regions of reference, where the Sr content is not visibly increased, numbered in black, have an average Sr content of 43.5 wt%. The averaged content of Sr of the entire particle (annotated as (1)–(3) in Figure 11a are 46, 44, and 43.4 wt% respectively. This confirms a local change in the chemical composition of these particles, which indicates that there are also phase transitions of the crystal phases according to the phase diagram from Sarver et al. [28].

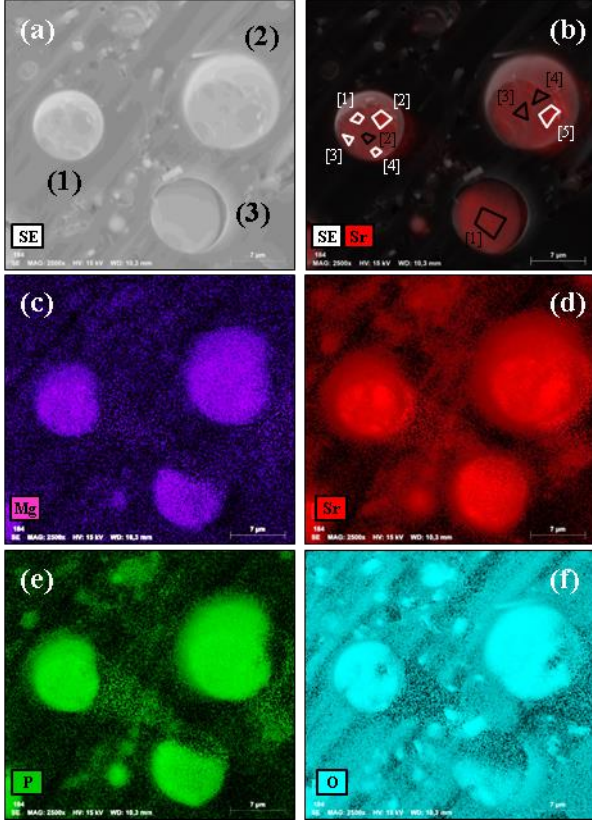


Figure 11: SE (a), SE+EDX for Sr (b) and EDX (c-f) images from a polished surface as a function of the respective chemical species (Sr, Mg, P, O). The highlighted regions in (b) are regions of high Sr content (white) and regular Sr content (black). Note that the EDX images (c-f) are not overlaid with SE images. The normalized Sr wt% are shown in Table 1.

Table 1: Normalized Sr content in various areas in the particle cross-section shown in Figure 11.

	1	2	3	4	5	\bar{x}
Sr high (wt%)	48	60	46	50	60	52.8
Sr low (wt%)	46	41	45	42	-	43.5

The X-ray diffraction pattern (Figure 12) from the initial material SMP:Sn (blue) matches well the those from β -phase (yellow diffraction peaks) of the $(\text{Sr},\text{Mg})_3(\text{PO}_4)_2$ when the mole fraction $\text{Mg}_3(\text{PO}_4)_2$ is between 10–35% [28]. Based on the EDX measurements of the initial material, the measured contribution of $\text{Mg}_3(\text{PO}_4)_2$ is 12.5 mol%. In the diffraction pattern of the post-flame SMP:Sn (diffraction pattern in the middle), the peaks from the $\beta\text{-Sr}_3(\text{PO}_4)_2$ are less pronounced, thus, the phases can only partially be attributed to the phases of the initial material.

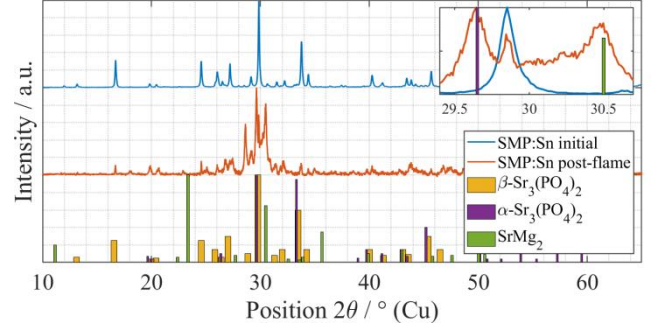


Figure 12: Diffraction pattern from initial and post-flame SMP:Sn phosphor material (top and center). The diffraction peaks (bottom) are visualized in different widths to improve visibility of closely adjacent peaks. Inset plot: enlargement from $2\theta = 29.4\text{--}30.6^\circ$.

Moreover, the presence of two new phases can be confirmed from the diffraction pattern of the post-combustion material, which are recognized as $\alpha\text{-Sr}_3(\text{PO}_4)_2$ and $\text{SrMg}_2(\text{PO}_4)_2$. The appearance of these two phases is highlighted in the inset plot in

Figure 12. Both phases also appear in the phase diagram of $(\text{Sr},\text{Mg})_3(\text{PO}_4)_2$ at different Mg mole fractions [28]. This will be discussed in detail in the following section. Due to the low quantity of recaptured phosphor, the interference scan of the post-flame SMP:Sn is carried out in transmission mode of the X-ray detector, leading to decreased sensitivity of the scan. Even if it is difficult to quantify the proportions of different phases in the post-combustion material, it is clear that the material had undergone phase change and that the crystal properties of the post-flame material are modified relatively to the initial material.

3.3. Discussion

The phosphor YAG:Pr enables temperature measurements in the post-combustion regime for various fuel/air equivalence ratios. The structural analysis of YAG:Pr does not show changes in the crystal structure after passing the flame front, where the adiabatic temperature is approximately 1900 K ($\phi = 0.71$). Even if melting is not expected for the majority of particles, isolated spherical particles are detected under these conditions (Figure 8), which indicates melting. Between this condition and the melting temperature of YAG (2213 ± 7 K [26]), no significant changes in luminescence properties of the post-flame material are expected. However, thermographic measurements were possible in the post-combustion gases even in stoichiometric flames ($\phi = 1.0$). An evaluation of the band-integrated luminescence relative to the volumetric particle number density derived from Mie-scattering showed no significant loss of per-particle luminescence. The adiabatic flame temperature is ~ 2350 K [31], thus melting can have occurred. We can, however, not finally conclude whether luminescence has recovered after solidification or if the particles did not melt because of

deviation from the adiabatic flame temperature due to heat losses.

For the second investigated phosphor, SMP:Sn, no phosphor luminescence is detected in the post-combustion regime. Based on the results presented above, two possible degradation paths are proposed, which can give rise to the observed loss of the luminescent properties of SMP:Sn after passing the material through the flame.

Firstly, the spectroscopic properties of SMP:Sn are related to the presence of Sn^{2+} . In a strongly oxidizing high-temperature environment, further oxidation of this species towards the less stable Sn^{4+} ion is expected [38]. In previous investigations, SMP:Sn was heated up three times to 900 K (20 K/min) but the luminescent properties did not show a difference towards the untreated sample [14]. Koelmans and Cox observed an 8 % luminescence reduction of $(\text{Sr}, \text{Mg})_3(\text{PO}_4)_2:\text{Sn}^{2+}$ after exposing the sample at 973 K to air for 15 min. The luminescence emission continuously decreased for longer storage time in air, up to a total loss of luminescence after 100 hours [27]. The authors did not specify the exact mole fraction of $\text{Mg}_3(\text{PO}_4)_2$ in the investigated $(\text{Sr}, \text{Mg})_3(\text{PO}_4)_2:\text{Sn}^{2+}$. However it was also shown that different Mg/Sr compositions of the host lattice do not affect the equilibrium between Sn^{2+} and Sn^{4+} but only the oxidation rate and thus the time until the loss of its luminescent properties [27]. In our experiment, the burner is operated in lean combustion ($\phi < 1$) to avoid soot formation and thus providing excess oxygen.

Secondly, the luminescent emission from phosphors strongly depends on the lattice structure [39]. Based on the EDX measurement from bulk powder, the mole fraction of $\text{Mg}_3(\text{PO}_4)_2$ in the lattice is measured to be 12.5 mol% in the initial material. According to the phase diagram of $(\text{Sr}, \text{Mg})_3(\text{PO}_4)_2$, this corresponds to the concentration of $\text{Mg}_3(\text{PO}_4)_2$, where the phosphor shows its maximum brightness in the phase of $\beta\text{-Sr}_3(\text{PO}_4)_2$ (10–15 mol% of $\text{Mg}_3(\text{PO}_4)_2$) [28]. The presence of this phase was determined by XRD measurements of the initial material (Figure 12). However, the adjacent phase, which is characterized by $\text{Mg}_3(\text{PO}_4)_2$ below ~10 mol%, contains the non-luminescent $\alpha\text{-Sr}_3(\text{PO}_4)_2$ [28]. Therefore, slight changes in the mole fraction of the Sr/Mg content can result in a total loss of luminescence.

The melting point of the mixed $\text{Sr}_3(\text{PO}_4)_2\text{-Mg}_3(\text{PO}_4)_2$ orthophosphate at the given lattice mole fraction is not exactly known. The melting point of pure $\text{Mg}_3(\text{PO}_4)_2$ is 1630 K [40]. The melting point of pure $\text{Sr}_3(\text{PO}_4)_2$ is also not exactly known, but can be assumed to be lower, as the crystal field strength of the Sr–O bond (2.641 Å) is lower than for the Mg–O bond (2.046 Å) [41]. Therefore, in the current experimental conditions, where the particles were recaptured

and analyzed ($\phi = 0.71$, $T_{\text{adiabatic}} \approx 1900$ K), at least partial melting is expected for SMP:Sn

During the cool-down, the orthophosphate can follow the phase boundary of the two-phase area ($\beta\text{-Sr}_3(\text{PO}_4)_2$ and liquid) and solidify in the adjacent two-phase region ($\beta\text{-Sr}_3(\text{PO}_4)_2$ and $\text{SrMg}_2(\text{PO}_4)_2$) according to the phase diagram [28]. Some peaks in the measured diffraction pattern of the post-flame SMP:Sn material can clearly be attributed to $\text{SrMg}_2(\text{PO}_4)_2$, which can be seen in the inset in Figure 12.

If the melting point is exceeded, mixed ternary orthophosphates, like the $(\text{Sr}, \text{Mg})_3(\text{PO}_4)_2$, tend also to break up into elementary phosphates [42]. At high Sr concentrations, this can result in the $\beta\text{-Sr}_3(\text{PO}_4)_2$ and the non-luminescent α -phase, both phases had also been found in the XRD analysis of the post-flame material. The inset in Figure 10 shows the decreased intensity of the β -phase and the presence of the $\alpha\text{-Sr}_3(\text{PO}_4)_2$, relative to the initial material. For low Sr concentrations, the phosphate $\text{Mg}_3(\text{PO}_4)_2$ can be amorphous and would thus not be visible in XRD analysis [28].

Optical measurements in the burner exhaust gases prevented temperature measurements due to the absence of detectable luminescence. X-ray diffraction analysis showed significant phase transition, where the $\text{SrMg}_2(\text{PO}_4)_2$ phase and the non-luminescent $\alpha\text{-Sr}_3(\text{PO}_4)_2$ phase was detected in the post-flame material. Based on the analysis presented here, it can be concluded that phase transformation of the $(\text{Sr}, \text{Mg})_3(\text{PO}_4)_2$ orthophosphate, induced by passing through the flame at the given conditions, is responsible for the entire loss of luminescence. Lastly, it should be noted that the melting temperature for the SMP:Sn material provided by the manufacturer (> 1473 K) is given for a particle size distribution between $d_{50} = 8 \dots 10 \mu\text{m}$. For temperature/velocity measurements using thermographic phosphors as tracer particles, the size distribution is usually reduced towards the low μm -range to ensure that the seeded particles follow changes in temperature and velocity [33]. Also, chemical reactivity increases at decreasing particle size due to the enlarged specific surface. Therefore, it is also possible that degradation processes like oxidation, which are disadvantageous for the luminescence yield of certain thermographic phosphors, e.g., $(\text{Sr}, \text{Mg})_3(\text{PO}_4):\text{Sn}^{2+}$ [26] are further increased or can occur earlier by reducing the particle size. However, if the limiting factor for particle survivability is the residence time above a certain temperature (e.g., melting temperature), it can be of particular interest to choose large particle diameters if this is permissible for the flow conditions in the region of interest (e.g., post-combustion gases), where temperature- and velocity gradients are less pronounced. This increases the thermal inertia and thus reaching of the melting temperature can be

avoided for reacting conditions with short time scales. It is shown that the response time increases significantly with increasing particle size (t_{95} increases from 27 μs for a particle size of 2 μm to 577 μs for 8 μm) [33].

4. Conclusions

The primary goal of this study was to investigate the suitability of two phosphors (YAG:Pr and SMP:Sn) for thermographic measurements in post-combustion gases, especially for studies in internal combustion engines. To emulate an optically-accessible combustion environment, a premixed propane/air flame was used at a wide range of fuel/air equivalence ratios ($\phi = 0.71-1$), which also changes the temperature of the exhaust gases. It was shown that YAG:Pr maintains its luminescence properties upon passing the reaction zone of the burner, enabling temperature measurements in the burnt-gas regime, based on the two-color intensity ratio approach. 2D temperature measurements of the post-combustion gases were determined for various equivalence ratios, up to a gas temperature of 890 K. Phosphor particles were recaptured downstream of the flame and analyzed using SEM/EDX and XRD. Microscopic measurements did not show changes in chemical composition, morphology or crystal structure for YAG:Pr relatively to the initial material. In contrast to YAG:Pr, the second investigated phosphor, SMP:Sn does not exhibit any remaining luminescence downstream of the reaction zone. The microscopic analysis of the post-flame phosphor material revealed that the material had melted in the flame and undergone crystal phase transformation towards different phases of the (Sr,Mg)-orthophosphate ($\alpha\text{-Sr}_3(\text{PO}_4)_2$ and $\text{SrMg}_2(\text{PO}_4)_2$).

This study shows that temperature measurements in the post-flame environment using thermographic phosphors are not only limited by its weak luminescence at elevated temperature as widely assumed, but also by materials decomposition, which can lead from decreasing luminescence to as far as an entire loss of the materials' luminescence properties. Further investigations of other phosphor materials need to be carried out to extend the measurable temperature range and to know restricting conditions of the respective thermographic phosphors. The constraints to experimental conditions can additionally be determined from thermodynamic modeling of the melting process to determine acceptable residence times for the respective materials in the given temperature field.

Acknowledgements

The authors thank Dr. Markus Suta (Utrecht University, Debye Institute for Nanomaterials Science) for the valuable

input and Dr. Ulrich Hagemann (ICAN, University of Duisburg-Essen) for his support in evaluating the EDX data. This work was supported by funding from the German Research Foundation within project 275255277.

References

- [1] Brübach J, Pflitsch C, Dreizler A and Atakan B 2013 On surface temperature measurements with thermographic phosphors: A review *Progress in Energy and Combustion Science* **39** 37–60
- [2] Abram C, Fond B and Beyrau F 2018 Temperature measurement techniques for gas and liquid flows using thermographic phosphor tracer particles *Progress in Energy and Combustion Science* **64** 93–156
- [3] Schulz C and Sick V 2005 Tracer-LIF diagnostics: Quantitative measurement of fuel concentration, temperature and fuel/air ratio in practical combustion systems *Progress in Energy and Combustion Science* **31** 75–121
- [4] Tea G, Bruneaux G, Kashdan J T and Schulz C 2011 Unburned gas temperature measurements in a surrogate Diesel jet via two-color toluene-LIF imaging *Proceedings of the Combustion Institute* **33** 783–90
- [5] Lee T, Bessler W G, Kronemayer H, Schulz C and Jeffries J B 2005 Quantitative temperature measurements in high-pressure flames with multiline NO-LIF thermometry *Appl. Opt.* **44** 6718–28
- [6] Bessler W G, Hildenbrand F and Schulz C 2001 Two-line laser-induced fluorescence imaging of vibrational temperatures in a NO-seeded flame *Appl. Opt.* **40** 748–56
- [7] Seitzman J M, Hanson R K, DeBarber P A and Hess C F 1994 Application of quantitative two-line OH planar laser-induced fluorescence for temporally resolved planar thermometry in reacting flows *Appl. Opt.* **33** 4000–12
- [8] Peukert S, Sallom A, Emelianov A, Endres T, Fikri M, Böhm H, Jander H, Eremin A and Schulz C 2019 The influence of hydrogen and methane on the growth of carbon particles during acetylene pyrolysis in a burnt-gas flow reactor *Proceedings of the Combustion Institute* **37** 1125–32
- [9] Witkowski D and Rothamer D A 2019 Scattering referenced aerosol phosphor thermometry *Measurement Science and Technology* **30** 44003
- [10] Hertle E, Bollmann J, Aßmann S, Kalancha V, Osvet A, Batentschuk M, Will S and Zigan L 2020 Characterization of the phosphor (Sr,Ca)SiAlN₃: Eu²⁺ for temperature sensing *Journal of Luminescence* **226** 117487
- [11] Herzog J M, Witkowski D and Rothamer D A 2021 Characterization of the Ce,Pr:LuAG phosphor for Co-doped aerosol phosphor thermometry *Journal of Luminescence* **229** 117665
- [12] Witkowski D and Rothamer D A 2019 A novel strategy to improve the sensitivity of aerosol phosphor thermometry using co-doped phosphors *Proceedings of the Combustion Institute* **37** 1393–400
- [13] Jordan J A R D A 2013 Pr:YAG temperature imaging in gas-phase flows *Applied Physics B* **110** 285–91
- [14] Fond B, Abram C, Pougin M and Beyrau F 2019 Investigation of the tin-doped phosphor (Sr,Mg)₃(PO₄)₂:Sn²⁺ for fluid

- temperature measurements *Optical Materials Express* **9** 802–18
- [15] Yin Z, Fond B, Eckel G, Abram C, Meier W, Boxx I and Beyrau F 2017 Investigation of BAM:Eu²⁺ particles as a tracer for temperature imaging in flames *Combustion and Flame* **184** 249–51
- [16] van Lipzig, J. P. J., Yu M., Dam N. J., Luijten C. C. M. and de Goey L. P. H. 2013 Gas-phase thermometry in a high-pressure cell using BaMgAl₁₀O₁₇:Eu as a thermographic phosphor *Applied Physics B* **111** 469–81
- [17] Hasegawa R, Sakata I., Yanagihara H., Johansson B., Omrane A. and Aldén M. 2007 Two-dimensional gas-phase temperature measurements using phosphor thermometry *Applied Physics B* **88** 291–6
- [18] Yu M, Särner G, Luijten C C M, Richter M, Aldén M, Baert R S G and de Goey L P H 2010 Survivability of thermographic phosphors (YAG:Dy) in a combustion environment *Measurement Science and Technology* **21** 37002
- [19] Neal N J, Jordan J and Rothamer D 2013 Simultaneous measurements of in-cylinder temperature and velocity distribution in a small-bore Diesel engine using thermographic phosphors *SAE International Journal of Engines* **6** 300–18
- [20] Kopf A, Bardi M, Endres T, Bruneaux G and Schulz C Temperature measurements in engine post-combustion gases using YAG:Pr³⁺: manuscript in preparation
- [21] Donegá C D M, Meijerink A and Blasse G 1995 Non-radiative relaxation processes of the Pr³⁺ ion in solids *Journal of Physics and Chemistry of Solids* **56** 673–85
- [22] Piper W W, DeLuca J A and Ham F S 1974 Cascade fluorescent decay in Pr³⁺-doped fluorides: Achievement of a quantum yield greater than unity for emission of visible light *Journal of Luminescence* **8** 344–8
- [23] Witkowski D and Rothamer D A 2017 Emission properties and temperature quenching mechanisms of rare-earth elements doped in garnet hosts *Journal of Luminescence* **192** 1250–63
- [24] Caslavsky J L and Viechnicki Dennis J. 1980 Melting behaviour and metastability of yttrium aluminium garnet (YAG) and YAlO₃ determined by optical differential thermal analysis *Journal of Materials Science* **15** 1709–18
- [25] Butler K H 1953 Alkaline Earth Orthophosphate Phosphors *Journal of The Electrochemical Society* **100** 250
- [26] Donker H 1989 On the Luminescence of Some Tin-Activated Alkaline-Earth Orthophosphates *Journal of The Electrochemical Society* **136** 3130
- [27] Koelmans H and Cox A P M 1957 Luminescence of Modified Tin-Activated Strontium Orthophosphate *Journal of The Electrochemical Society* **104** 442
- [28] Sarver J F, Hoffman M V and Hummel F A 1961 Phase Equilibria and Tin-Activated Luminescence in Strontium Orthophosphate Systems *Journal of The Electrochemical Society* **108** 1103
- [29] OSRAM GmbH 2011 Material safety data sheet (SDS): Phosphor SV 253: Strontiummagnesiumorthophosphate: tin activated (#B4640219). OSRAM GmbH (Munich)
- [30] Fond B, Abram C, Pougin M and Beyrau F 2019 Characterisation of dispersed phosphor particles for quantitative photoluminescence measurements *Optical Materials* **89** 615–22
- [31] Kennel C, Göttgens J and Peters N 1991 The basic structure of lean propane flames *Symposium (International) on Combustion* **23** 479–85
- [32] Mechanical and Aerospace Engineering (Combustion Research), University of California at San Diego 2016 *Chemical-Kinetic Mechanisms for Combustion Applications: San Diego Mechanism web page* <https://web.eng.ucsd.edu/mae/groups/combustion/mechanism.html>
- [33] Fond B, Abram C, Heyes A L, Kempf A M and Beyrau F 2012 Simultaneous temperature, mixture fraction and velocity imaging in turbulent flows using thermographic phosphor tracer particles *Opt. Express* **20** 22118–33
- [34] Zentgraf F, Stephan M, Berrocal E, Albert B, Böhm B and Dreizler A 2017 Application of structured illumination to gas phase thermometry using thermographic phosphor particles: A study for averaged imaging *Experiments in Fluids* **58** 82
- [35] Kopf A, Bardi M, Bruneaux G, Fond B, Endres T and Schulz C The potential of (Sr,Mg)₃(PO₄)₂:Sn²⁺ for gas-phase phosphor thermometry in post-combustion gases. *Poster presented at: 37th International Symposium on Combustion, 2018; Dublin, Ireland*
- [36] Yoder H S and Keith M 1950 Complete substitution of aluminum for silicon: The system (MnO)₃Al₂O₃(SiO₂)₃—(Y₂O₃)₃(Al₂O₃)₅ *Geological Society of America, Bulletin* 1516–7
- [37] Gražulis S, Chateigner D, Downs R T, Yokochi A F T, Quirós M, Lutterotti L, Manakova E, Butkus J, Moeck P and Le Bail A 2009 Crystallography Open Database - an open-access collection of crystal structures *Journal of Applied Crystallography* **42** 726–9
- [38] Riedel E and Janiak C 2015 *Anorganische Chemie* (Berlin, Boston: De Gruyter)
- [39] Blasse G and Grabmaier B C 1994 *Luminescent Materials* (Berlin, Heidelberg: Springer Berlin Heidelberg)
- [40] Berak J 1958 The System Magnesium Oxide - Phosphorus Pentoxide *Roczniki chemii* **32** 17–22
- [41] Li K, Chen D, Zhang R, Yu Y and Wang Y 2013 Eu²⁺:SrMg_{1-x}Mn_xP₂O₇ (x = 0–1) phosphors with tunable yellow–red emissions *Journal of Alloys and Compounds* **555** 45–50
- [42] Wiberg N, Holleman A F, Wiberg E and Fischer G 2008 *Lehrbuch der Anorganischen Chemie* (Berlin, Boston: De Gruyter)